Applied Surface Science 636 (2023) 157792

Contents lists available at ScienceDirect

Applied Surface Science

journal homepage: www.elsevier.com/locate/apsusc

Full Length Article

Insights into reaction pathway induced by d orbital occupancy on cobalt supported boron nitride for N_2O catalytic decomposition

Wenqiang Qu, Chunlei Wang, Penglu Wang, Yongjie Shen, Jiebing He, Dengsong Zhang *

International Joint Laboratory of Catalytic Chemistry, College of Sciences, Shanghai University, Shanghai 200444, China

ARTICLE INFO

Keywords:
Environmental chemistry
N_2O catalytic decomposition
Reaction pathway
D orbital occupancy
Density functional theory (DFT)

ABSTRACT

Nitrous oxide (N_2O), as a typical greenhouse gas, is urgent to be eliminated to address the global climate issue. Developing low-temperature N_2O decomposition catalysts is crucial for mitigating greenhouse gas emissions. Herein, we propose a Cobalt-supported boron nitride (Co-BN) catalyst with a low reaction energy barrier (1.37 eV) using density functional theory calculations. The coordination environment is critical to the reaction mechanism and energy barrier, where the CoN_3 configuration (Co coordinated with three N atoms) triggers the Eley-Rideal (E-R) mechanism, but the CoB_3 configuration (Co coordinated with three B atoms) engenders the Langmuir-Hinshelwood (L-H) mechanism. Fundamentally, the reaction mechanism is dominated by d orbital occupancy. Following the adsorption of *O intermediate, a fully filled d orbital is realized on *O-CoN_3, which prevents N_2O from bonding with Co, thus following the E-R mechanism through directly interacting with *O specie. Conversely, the partially unoccupied d orbital is identified on *O-CoB_3, provinding the bonding site on Co for N_2O molecule, thereby leading to the L-H mechanism. Our work provides a novel N_2O decomposition catalyst theoretically, and the insights into the relationship between d orbital occupancy and the reaction mechanism, would pave a new avenue for the design of N_2O decomposition catalysts.

1. Introduction

Nitrous oxide (N_2O) is the primary contributor to stratospheric ozone depletion and ranks as the third-largest greenhouse gas emitter [1,2]. In recent years, the concentration of N_2O in the atmosphere has displayed a persistent upward trend attributed to excessive anthropogenic emissions. Despite 75% of anthropogenic N_2O emissions being released into the atmosphere due to agricultural soil management, significant emissions still arise from industrial production processes (such as nitric acid and adipic acid production) as well as fossil fuel combustion originating from stationary and mobile sources [3–6]. Alarming statistics indicate that an astounding 0.9 million tons of N_2O are annually released into the atmosphere due to industrial activity alone [4]. Furthermore, projections suggest that N_2O emissions will reach a staggering 1.4 million tons per year by 2050 [7,8]. In response to the environmental and climatic consequences resulting from the mounting N_2O emissions, numerous pollution control technologies have been developed [9–12]. Among them, direct catalytic decomposition of N_2O has emerged as the most promising technique for mitigating N_2O emissions in the industrial sector [13,14].

Due to its highly stable molecular structure, the thermo-catalytic decomposition of N_2O molecules typically necessitates high temperatures, resulting in increased operation costs and posing significant challenges to the high-temperature thermal stability of the catalysts [15]. Over time, a plethora of N_2O-decomposition catalysts have been experimentally developed, and can be classified into three categories: noble-metal-supported catalysts, metal oxides, and zeolite-based catalysts [16–19]. While noble-metal-supported catalysts exhibit excellent low-temperature activity, their limited natural abundance makes them prohibitively expensive for large-scale use [20,21]. Conversely, metal oxides and zeolite-based catalysts are more affordable, but they display inferior low-temperature activity [22–25]. Therefore, discovering and developing innovative N_2O-decomposition catalysts with low-temperature activity is of utmost importance.

To develop newly promising catalysts, theoretical techniques are utilized to predict their properties in N_2O decomposition [26,27]. It has been observed that metallic sites with low oxidation states are advantageous for N_2O decomposition [28,29]. As a result, researchers are investigating catalytic systems with abundant electronic states [30,31]. Previously, our work has reported the N_2O decomposition on metal-site

* Corresponding author.
E-mail address: dszhang@shu.edu.cn (D. Zhang).

https://doi.org/10.1016/j.apsusc.2023.157792
Received 23 April 2023; Received in revised form 5 June 2023; Accepted 13 June 2023
Available online 17 June 2023
0169-4332/© 2023 Elsevier B.V. All rights reserved.

catalysts supported by non-metallic materials [32], and the Ti-porphyrin catalysts was determined to exhibit exceptional catalytic activity through theoretical investigations. Subsequently, Vakili et al. [33] investigated the N_2O decomposition on metal-graphene catalysts and found that silicon-embedded graphene catalysts have high potential for practical application. In contrast to conventional metal oxide and zeolite supports, nonmetallic supports display moderate electronegativity, which effectively regulates the electronic structure of metallic sites [34]. However, both porphyrin and graphene-like nonmetallic supports have poor thermal stability, which significantly limits their practical use.

Herein, the boron nitride (BN) material with high thermal stability and abundant surface electrons was utilized as the supports [35], and the catalytic decomposition of N_2O was investigated on Co-supported BN materials (Co-BN). A low reaction energy barrier (1.37 eV) was revealed on Co-BN. Furthermore, the reaction mechanism was found to be strongly correlated with the coordination environment of Co. Specifically, the N_2O molecule underwent an Eley-Rideal (E-R) mechanism on the CoN_3 structure (three N-coordinated Co sites) and a Langmuir-Hinshelwood (L-H) mechanism on the CoB_3 structure (three B-coordinated Co sites). The different mechanism was determined by the filling degree of d orbitals on Co, which can be adjusted by the intermediate *O. This study developed a promising catalyst for N_2O decomposition and provides a theoretical understanding of the structure–activity relationship between coordination configuration and reaction pathways, which will guide the future design of N_2O decomposition catalysts.

2. Computational methods

The Vienna ab initio Simulation Package (VASP) was used to perform all spin-polarized DFT calculations [36], and generalized gradient approximation (GGA) based Perdew-Burke-Ernzerhof (PBE) functional was employed to treat the exchange–correlation effects [37]. The DFT-D3 method was employed for dispersion corrections. The plane wave energy cutoff was set to 500 eV. The initial hexagonal BN model with the P63/MMC space group was obtained from the Inorganic Crystal Structure Database (ICSD), and the Gamma-centered K-Point grids of 12 × 12 × 12 were employed for the cell optimization. A BN supercell (7 × 7) consisting of 112 atoms (56 boron atoms and 56 nitrogen atoms) was constructed. A vacuum space of 15 Å was added perpendicular to the surface to avoid interactions between periodic images. A Gamma-centered K-Point grid of 1 × 1 × 1 was used for its geometry optimization, while the Gamma-centered K-Point grids of 2 × 2 × 1 was employed for the calculation convergence and electronic analysis, such as Bader charge analysis, crystal orbital Hamilton population, and density of states. On-site Coulomb interaction was addressed with the DFT + U method using U-J parameters of 3.3 eV for Co 3d [38]. The geometry optimizations were conducted with force and energy convergences of 0.02 eV/Å and 10^{-5} eV, respectively.

The adsorption energy of gas molecule was calculated using the formula: $E_a = E_{total} - (E_{slab} + E_{gas\text{-}molecule})$, where E_{total}, E_{slab} and $E_{gas\text{-}molecule}$ represent the corresponding energies of adsorption structure, catalyst, and gas molecule, respectively. To calculated the reaction barriers, we utilized the climbing image-nudge elastic band (CI-NEB) method with four intermediate images, which enabled us to identify the minimum energy pathway. The vibrational frequencies of adsorbates were calculated by finite-displacement method, where the slab atoms were all fixed, and only the adsorbate atoms were relaxed. The Gibbs free energy temperature corrections were theoretically calculated by the following equation:

$$\Delta G = \Delta E + \Delta ZPE - T\Delta S$$

Where ΔG represented the change in the Gibbs free energy, ΔE was the change in the adsorption energy, ΔZPE was the change in the zero-point energy, ΔS was the change in the entropy, and T was the reaction temperature. In this paper, the ΔG value can be obtained using the post-processing program of VASPKIT [39].

3. Results and discussions

To investigate the catalytic decomposition of N_2O using Co supported on BN, we examined two different coordination configurations: Co combined with three N atoms or three B atoms, which were labeled as CoN_3 and CoB_3, respectively. (The optimized structural models were presented in Fig. S1).

3.1. N_2O catalytic decomposition process

The entire process of N_2O decomposition was then calculated on CoN_3 catalyst, as illustrated in Fig. 1. Firstly, the decomposition process of the initial N_2O molecule (denoted as $^{(1)}N_2O$) was calculated. $^{(1)}N_2O$ molecule can be adsorbed on the Co site through either the O-terminal or N-terminal. According to the results of Gibbs free energy, both adsorption configurations were thermodynamically favorable. Following adsorption, the $^{(1)}N_2O$ molecule would undergo a rotation and bending process to complete the decomposition into N_2 and *O species, which corresponded to the first transition state process (TS1-O and TS1-N). Notably, although $^{(1)}N_2O$ adsorption at the N-terminal got a lower free energy, its decomposition energy barrier (1.49 eV) was significantly higher than that of the O-terminal adsorption pathway (0.54 eV). Due to the substantially lower activation energy barrier, the $^{(1)}N_2O$ molecule preferred to be activated with the form of O-terminal adsorption.

Following the release of N_2 molecule, the $^{(1)}N_2O$ molecule left behind an adsorbed O atom on the catalyst, resulting in the formation of *O-CoN_3, as depicted in process III. Subsequently, the second N_2O molecule (labled as $^{(2)}N_2O$) would continue to decompose on *O-CoN_3. The $^{(2)}N_2O$ molecule would directly attack the O atom on *O-CoN_3, leading to an Eley-Rideal (E-R) reaction[40], where $^{(2)}N_2O$ reacted without

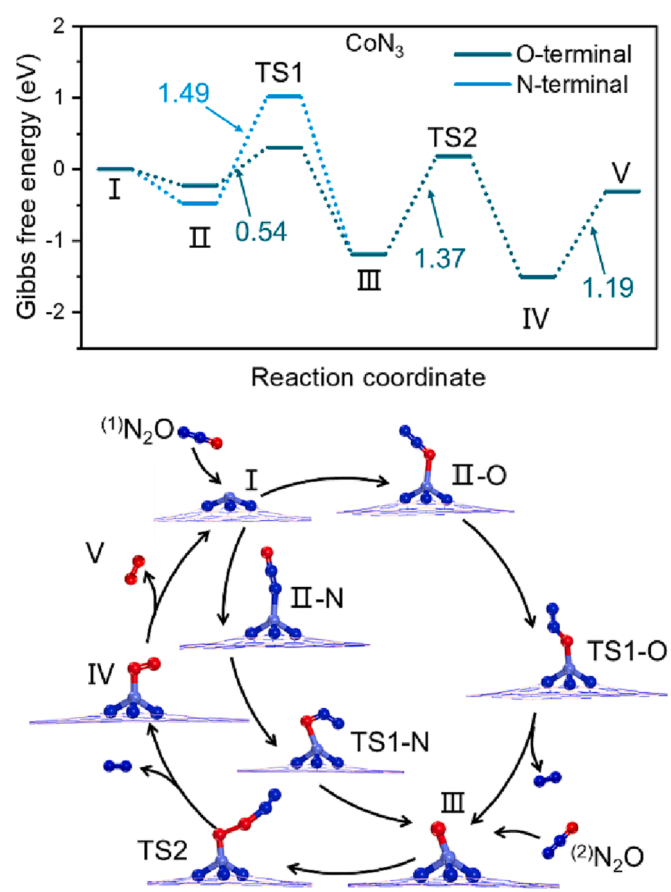

Fig. 1. The reaction Gibbs free energy diagrams for N_2O catalytic decomposition on CoN_3 catalyst.

adsorption, but directly with *O specie, as shown in process TS2. During this process, the $^{(2)}N_2O$ molecule was required to overcome the potential field generated by the catalyst, resulting in an activation energy barrier of 1.37 eV. Upon reaction of $^{(2)}N_2O$ with the *O species, the N_2 molecule was then released, while the O_2 molecule remained on CoN_3, as displayed in process IV. Finally, the O_2 molecule desorbed from the Co site, enabling the realization of the catalytic cycle on CoN_3 catalyst. The desorption process (IV-V) necessitated overcoming the chemisorption of the catalyst, with an energy barrier of 1.19 eV.

Therefore, three reaction barriers were involved during the catalytic cycle of N_2O decomposition on CoN_3. Among them, the rate-determined step of the entire reaction was assigned to the TS2 with the E-R reaction process, which exhibited the highest energy barrier (1.37 eV). Notably, since the calculations were performed at 0 K, the Gibbs free energy temperature correction was applied to the reaction (Fig. S2), and the results showed that, regardless of the temperature, TS2 process remained the rate-determined step.

The N_2O decomposition process on the CoB_3 was further investigated, as depicted in Fig. 2. Similar to the situation observed on CoN_3, the $^{(1)}N_2O$ molecule can be adsorbed on CoB_3 via the O-terminal or N-terminal, and both processes occurred spontaneously. Furthermore, during the activation process (TS1-O or TS1-N), the $^{(1)}N_2O$ dissociation energy barrier for O-terminal adsorption (0.71 eV) was lower than that of N-terminal adsorption (0.93 eV), indicating that N_2O was more readily adsorbed and dissociated with the O-terminal route.

The *O-CoB_3 (process III) was then formed after the $^{(1)}N_2O$ dissociation. Afterward, the adsorption and dissociation of the $^{(2)}N_2O$ molecule on the *O-CoB_3 occurred, as illustrated in TS2 process. The $^{(2)}N_2O$ molecule was adsorbed on the Co site of *O-CoB_3, and a small energy barrier (0.14 eV) was required for the TS2 process, much smaller than

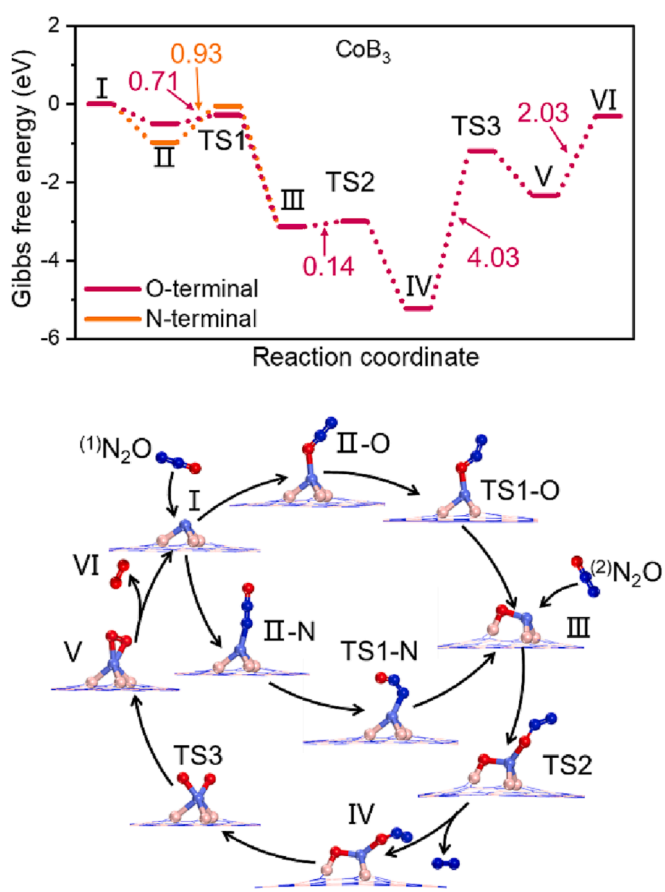

Fig. 2. The reaction Gibbs free energy diagrams for N_2O catalytic decomposition on CoB_3 catalyst.

that needed for the dissociation of the $^{(1)}N_2O$ molecule. After the dissociation, two adsorbed oxygen atoms were left on either side of Co site, as displayed in IV process. Subsequently, the two oxygen atoms overcame a higher energy barrier of 4.03 eV (TS3 process) to form the O_2 molecules on the Co sites (V process). Finally, the adsorbed O_2 molecule desorbed by overcoming the chemisorption of Co, which required a free energy of 2.03 eV, enabling the CoB_3 to refresh the catalyst.

Hence, among the four free energy-rising barriers observed in the catalytic cycle of N_2O decomposition on CoB_3, the formation of O_2 molecules from two adsorbed O atoms presented the highest energy barrier. The entire reaction of the N_2O decomposition on CoB_3 followed the L-H mechanism [41]. The temperature-corrected Gibbs free energy data (Fig. S3) revealed that regardless of the temperature, the rate-determined step of the overall reaction relied on the formation of O_2 under different temperatures.

In summary, the rate-determing step of N_2O decomposition reaction on CoN_3 was the dissociation of $^{(2)}N_2O$ molecule. The reaction proceeded through E-R mechanism, and the overall energy barrier was 1.37 eV. In contrast, on the CoB_3 conterpart, the rate-determining step was the formation of O_2 molecules from two adsorbed O atoms, and the reaction followed L-H mechanism, with an energy barrier of 4.03 eV. It was worth noting that the energy barrier for N_2O decomposition on CoN_3 catalyst was lower than numberous reported catalysts (Table S1), indicating that it delivered the promising potential as an efficient N_2O decomposition catalyst.

3.2. Electronic structure of Co

The distinct reaction mechanisms were exhibited under different coordination on BN supports. To get a deep insight of the relationship between the coordination structure of Co and the reaction mechanism, the d orbital structures of Co sites on both CoB_3 and CoN_3 catalysts were analyzed. As depicted in Fig. 3a, a significant number of spin-down unoccupied d orbitals were exhibited on CoN_3, and the charges of the up-spin and down-spin orbitals were asymmetric, indicating the vacancies in d orbitals on the CoN_3. Additionally, the lowest unoccupied orbital (LUMO) energy level was located at 0.75 eV. In contrast, the d orbitals of CoB_3 were displayed in Fig. 3b, and the symmetric up-spin and down-spin orbitals were confirmed, without any magnetic moment for Co atom. The occupied orbitals of CoB_3 were highly localized with electrons at the energy levels of −0.24 eV and −1.17 eV. However, few unoccupied orbitals were found on CoB_3, and the LUMO energy level was situated at 2.07 eV. The calculations without using the DFT + U method were also operated (Fig. S4 and Table S2), and the orbital distributions exihibited the same features compared to the calculations with the Hubbard correction.

Based on the N_2O decomposition process on CoN_3 and CoB_3, it was evident that the different reaction mechanisms (E-R and L-H) were determined by the geometry and electronic structure of *O at the Co site. To investigate the adsorption of *O on CoN_3 and CoB_3, the bonding interaction between the *O atom and other atoms on the catalyst was analyzed by crystal orbital Hamilton population (COHP) curves[42], and the bonding strenth can be determined by its corresponding integrated COHP (ICOHP) values, where a more negative ICOHP value indicated a stronger bonding strength beween the atoms. As depicted in Fig. 4a and 4b. the COHP between *O and Co atoms on CoN_3 was investigated and the ICOHP value was determined to be −5.96, while the ICOHP value between *O and N (connected to the Co site) was calculated as −0.24. The bonding interaction between *O and atoms on CoB_3 was then also investigated, as shown in Fig. 4c and 4d. the ICOHP value between *O and Co atom on CoB_3 was −2.84, while the value between *O and B was to be −11.27, indicating a strong interaction between *O and the support.

The bonding behavior of *O on CoN_3 and CoB_3 was analyzed by plotting the -ICOHP value between *O and N (or B) as the abscissa and the -ICOHP value between *O-Co as the ordinate. As depicted in Fig. 5a,

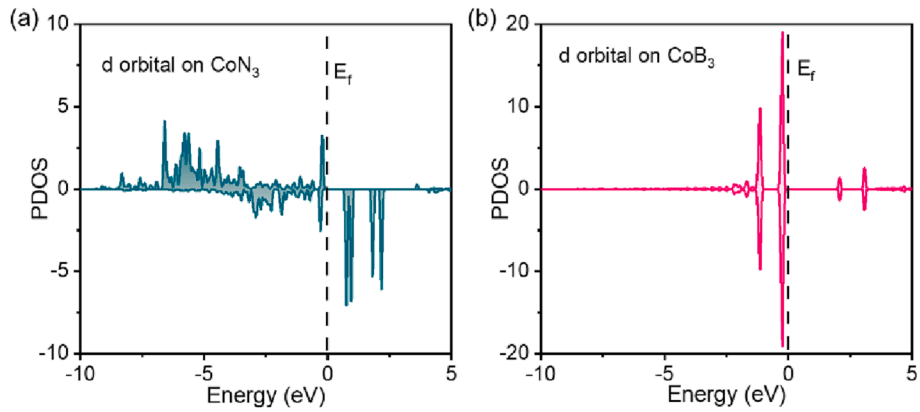

Fig. 3. Projected density of states (PDOS) profiles of d orbital on (a) CoN_3 and (b) CoB_3 catalysts.

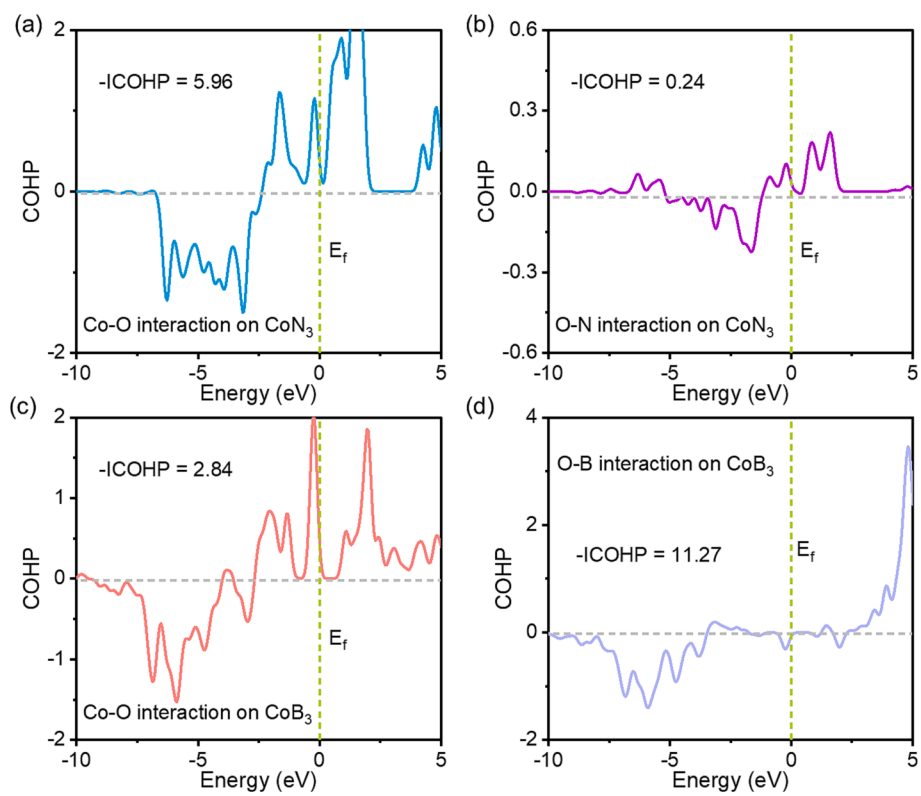

Fig. 4. Projected crystal orbital Hamilton population (pCOHP) between the adsorbed O atom and the surface (a) Co atom on CoN_3, (b) adjacent N atom on CoN_3, (c) Co atom on CoB_3, (d) adjacent B atom on CoB_3.

the bonding between *O and Co sites on CoN_3 exhibited a dominant role, signifying that Co sites primarily dictated the behavior of *O on CoN_3. Conversely, the bonding between *O and B on CoB_3 was dominant, indicating that the support played a crucial role in determining the behavior of *O on CoB_3.

To get a deeper insight into the interaction between *O and Co sites, the COHP curve between specific d orbitals on Co and *O was analyzed. The ICOHP values between each d orbital and the *O were shown in Fig. 5b. Interestingly, the interaction beween Co and *O on CoN_3 was mainly contributed by the d_{yz}, d_{xz}, and d_z^2 orbitals of Co. Due to the dominance of z-direction-related orbitals, the *O adsorbed above Co in the form of an axial oxygen. Differently, the interaction between Co and *O was mainly contributed by the d_{xy} and d_{xy}^2 orbitals on CoB_3, and a less effect was refected by the z-related d orbitals, leading to the adsorption of *O at the side position of Co.

Therefore, the distinctive d orbital contributions on CoN_3 and CoB_3 led to a different spatial distribution of *O adsorption on Co sites. Specifically, *O was adsorbed on the axial direction of Co site on CoN_3, which spatially avoided the contact of the $^{(2)}N_2O$ molecule with the Co site, resulting in the E-R mechanism. Conversely, *O was adsorbed on CoB_3 in a side direction to Co, providing sufficient space for $^{(2)}N_2O$ molecule to adsorb on the Co site, thereby creating a favorable condition for the L-H mechanism.

3.3. d orbital occupancy

In order to investigate the effect of O adsorption on the d orbitals, the d orbitals were then analyzed on *O-CoN_3. The z-direction-related orbitals were shown in Fig. 6a–c, and the results showed that after *O adsorption, the asymmetric up-spin and down-spin orbitals on CoN_3 were changed into symmetric on *O-CoN_3. Conversely, a contrasing phenomenon was observed for *O-CoB_3. As depicted in Fig. 6d–f, the

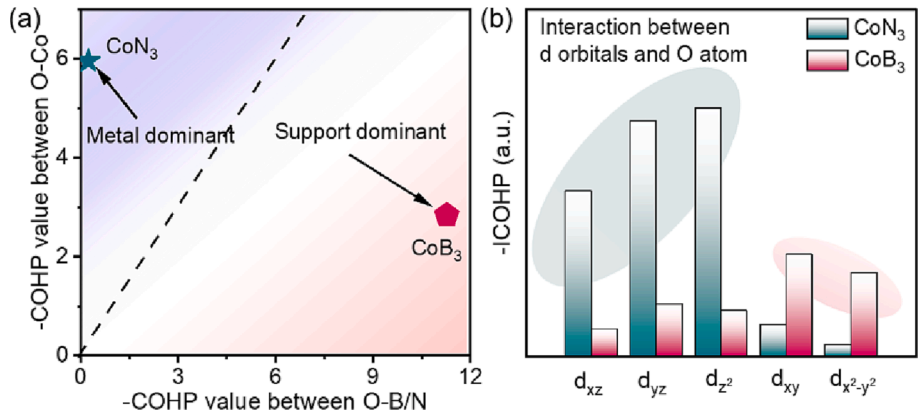

Fig. 5. (a) The interaction diagram between *O and the Co-BN catalyst. The abscissa is plotted by -ICOHP value between *O and N (or B), and the ordinate represents the -ICOHP value between *O and Co atom. (b) The ICOHP values between each d orbitals of Co and the adsorbed O atom.

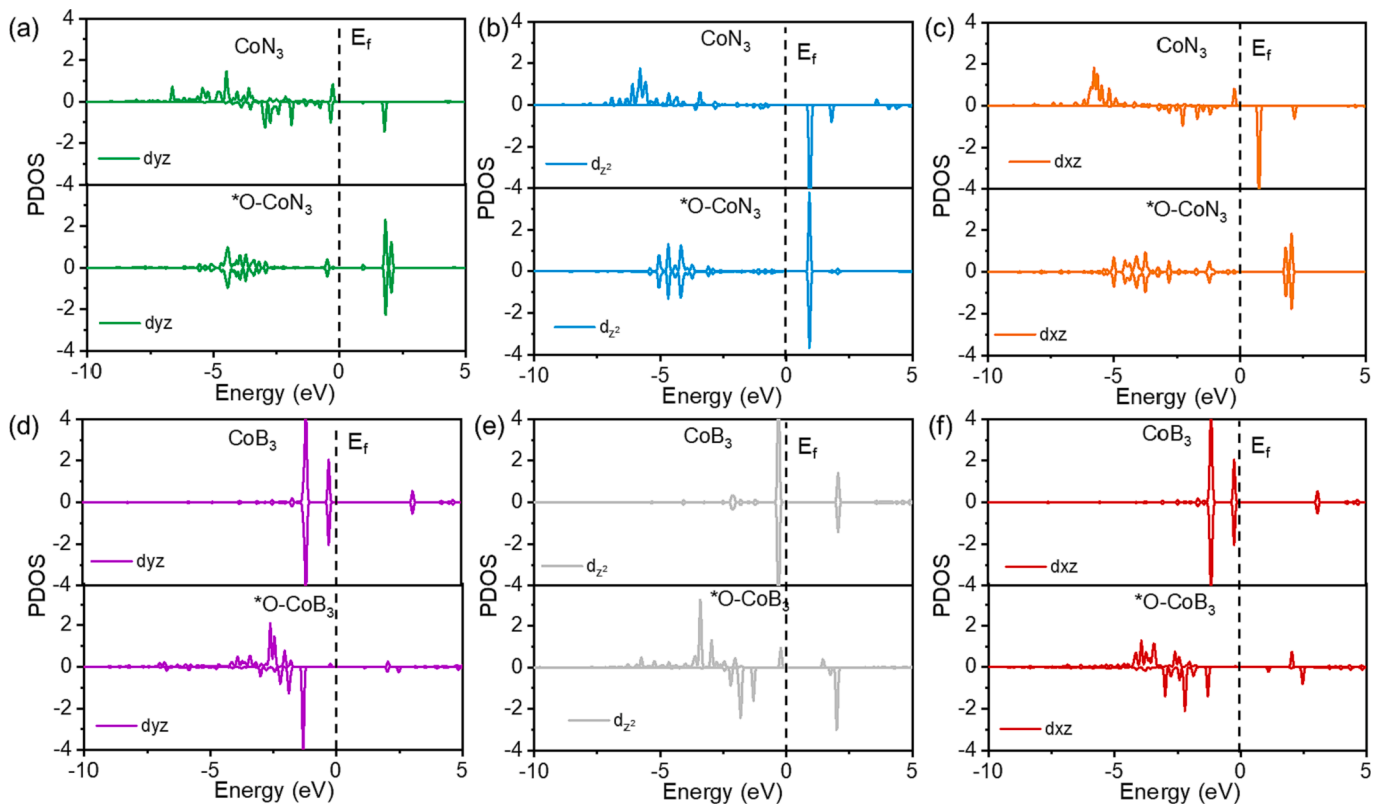

Fig. 6. The d orbitals of (a) d_{yz}, (b) d_z^2, and (c) d_{xz} on CoN_3 catalyst before and after *O specie adsorption. The d orbitals of (c) d_{yz}, (b) d_z^2, and (c) d_{xz} on CoB_3 catalyst before and after *O specie adsorption.

symmetric up-spin and down-spin orbitals on CoB_3 become asymmetric on *O-CoB_3. The opposite trend in orbital changes implies the crucial role of *O in regulating the d orbitals.

The number of valence electrons in CoN_3 and *O-CoN_3 were then analyzed by Bader charge analysis (Table S3) [43]. The valence electrons were revealed to be 7.82 e on *O-CoN_3, which was identical to that on CoN_3 (7.82 e), indicating that the bonding of *O did not affect the valence state of Co. Based on proceeding results, it can be concluded that despite with same number of valence electrons, the d orbitals of CoN_3 and *O-CoN_3 exhibited completely different distributions.

To determine the electron distribution of the d orbitals in CoN_3, the number of occupied electrons were calculated by integrated projected density of states (PDOS) of each orbitals. The results showed that few occupied electrons were exhibited on 4s orbital for CoN_3 (Table S4), indicating that the degenerate orbital arrangement of 4s on CoN_3 was $4s^0$. The up-spin orbitals of all d orbitals were fully occupied, while the down-spin orbitals were partially occupied. Since the number of valence electrons of Co was 7.82 e, the degenerate orbital arrangement of 3d was $3d^8$.

The valence orbital of *O-CoN_3 was then analyzed, and the 4s orbital still exhibited low electron occupantion (Table S5), indicating that its degenerate orbital arrangement remained at $4s^0$. For the symmetric up-spin and down-spin d orbitals on *O-CoN_3, although with the equal number of valence electrons, the arrangement of electrons in the 3d orbital had undergone significant changes before and after *O adsorption. As illustrated in Fig. 7a, two unpaired electrons would be generated under the electron arrangement of $3d^8$ configuration on CoN_3. However, when *O formed an inner-orbital coordination with Co, the $3d^8$ electrons

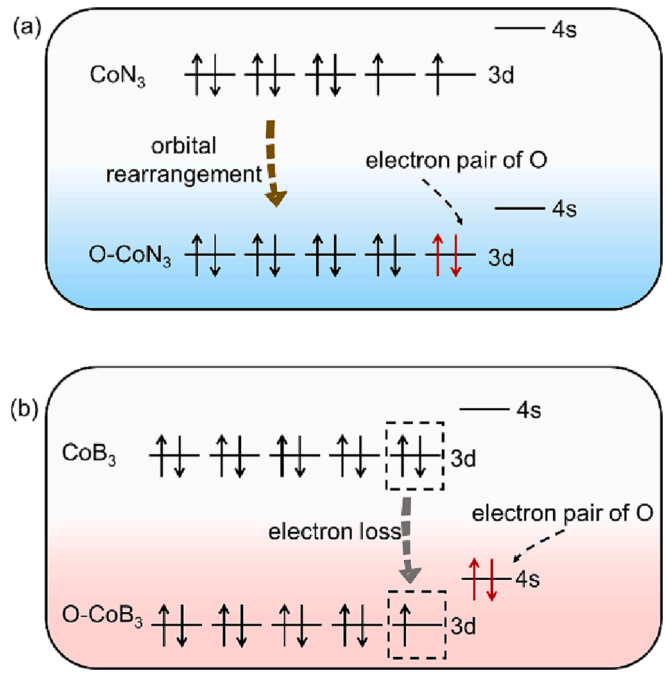

Fig. 7. Schematic illustration of orbital arrangement before and after O specie adsorption on (a) CoN_3 and (b) CoB_3 catalysts.

will rearrange to fill four d orbitals, leaving an empty orbital to coordinate with the lone pair of *O electrons. As a result, the asymmetric up-spin and down-spin orbitals on CoN_3 were changed into symmetric on *O-CoN_3.

Furthermore, the electron arrangement of CoB_3 and *O-CoB_3 were also investigated. Bader charge analysis (Table S6) showed that the number of valence electrons of Co on CoB_3 was calculated as 9.46 e, which was even higher than the element Cobalt ($3d^7 4s^2$). In addition, a low 4s orbital occupancy on CoB_3 revealed a $4s^0$ arrangement, and the symmetric up-spin and down-spin orbitals was resulted from the $3d^{10}$ arrangement (Table S7). Due to the back-donation electrons from the B 2p to Co 3d, the valence-electrons number of Co on CoB_3 exceeded the element Cobalt. Consequently, the Co electron arrangement on CoB_3 was $3d^{10}4s^0$.

For the situation on *O-CoB_3, the Bader charge results comfirmed a lower valence-electrons number than that on CoB_3, indicating the charge transfer between *O and Co. The 4s orbital configuration remained at $4s^0$, while the 3d orbital arrangement changed into $3d^9$, which resulted in the asymmetric up-spin and down-spin d orbitals on *O-CoB_3 (Table S8). As shown in Fig. 7b, the originally full 3d orbital electrons on CoB_3 would lose an electron under the *O adsorption, and the lone pair of *O would coordinate with the 4s empty orbital of Co, leading to the partially unoccupied d orbitals on *O-CoB_3.

Therefore, the orbital occupancy of CoN_3 and CoB_3 catalysts can be regulated by *O species, as illustrated in Fig. 8. In the case of CoN_3, *O can induce electron rearrangement and coordinate with empty orbitals to form fully filled d orbitals, which prevented N_2O molecules from effectively adsorbing on Co sites. Consequently, N_2O molecules tended to interact with *O, leading to the E-R reaction mechanism. On the other hand, in CoB_3, charge transfer occurred between *O and Co site, whereby one d-orbital electron was taken. The *O specie was then coordinated with the empty 4s orbital, leading to the fully filled d orbital into partially unoocupaied orbital, which allowed N_2O molecules to interact with the Co site through electron orbital bonding and thus facilitated the L-H mechanism. Therefore, a theoretical understanding of the structure–activity relationship between coordination configuration and reaction pathways based on Co supported boron nitride catalysts for N_2O decomposition was elaborately investigated, which will pave new

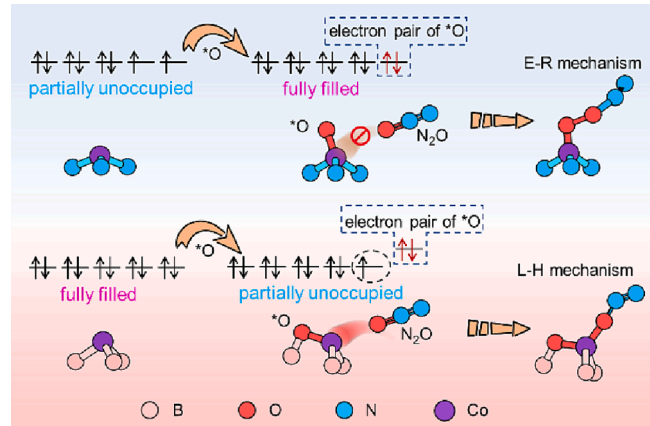

Fig. 8. Schematic illustration for the orbital-occupancy induced reaction mechanisms on CoN_3 and CoB_3 catalysts.

ways for the design of highly efficient N_2O decomposition catalysts.

4. Conclusion

The catalytic decomposition of N_2O is an essential technique for reducing greenhouse gas emissions. However, the challenge of high operating temperatures makes it crucial to develop N_2O decomposition catalysts that exhibit low-temperature activity. In this study, we have employed theoretical predictions to identify Co-supported BN catalysts with low reaction energy barriers and high potential for N_2O decomposition. Furthermore, the Co coordination configuration is found to be closely related to the reaction mechanism, where the CoN_3 configuration (Co coordinate with three nitrogen atoms) triggers the E-R reaction mechanism, but the CoB_3 configuration (Co coordinate with three boron atoms) leads to the L-H mechanism. The distinct reaction mechanisms are attributed to the d orbital occupancy degree of Co, and the adsorbed *O intermediate species can adjust the occupancy of orbitals. This work provides a theoretical prediction of a new type of N_2O decomposition catalyst, and the insights into the relationship between d orbital occupancy and the reaction mechanism, would pave a new avenue for the design of N_2O decomposition catalysts.

CRediT authorship contribution statement

Wenqiang Qu: Investigation, Data curation, Formal analysis, Writing – original draft. **Chunlei Wang:** Investigation, Formal analysis, Writing – review & editing. **Penglu Wang:** Formal analysis, Writing – review & editing. **Yongjie Shen:** Methodology, Investigation. **Jiebing He:** Methodology, Investigation. **Dengsong Zhang:** Investigation, Validation, Conceptualization, Writing – review & editing, Funding acquisition.

Declaration of Competing Interest

The authors declare that they have no known competing financial interests or personal relationships that could have appeared to influence the work reported in this paper.

Data availability

Data will be made available on request.

Acknowledgements

This work was financially supported by the National Natural Science Foundation of China (22125604).

Appendix A. Supplementary material

Supplementary data to this article can be found online at https://doi.org/10.1016/j.apsusc.2023.157792.

References

[1] X. Su, L. Yang, K. Yang, Y. Tang, T. Wen, Y. Wang, M.C. Rillig, L. Rohe, J. Pan, H. Li, Y.-G. Zhu, Estuarine plastisphere as an overlooked source of N_2O production, Nat. Commun. 13 (2022) 3884, https://doi.org/10.1038/s41467-022-31584-x.

[2] A.R. Ravishankara, J.S. Daniel, R.W. Portmann, Nitrous oxide (N_2O): The dominant ozone-depleting substance emitted in the 21st century, Science 326 (2009) 123–125, https://doi.org/10.1126/science.1176985.

[3] E. Tabor, G. Sádovská, M. Bernauer, P. Sazama, J. Nováková, V. Fíla, T. Kmječ, J. Kohout, K. Závěta, Z. Sobalík, Feasibility of application of iron zeolites for high-temperature decomposition of N_2O under real conditions of the technology for nitric acid production, Appl. Catal. B 240 (2019) 358–366, https://doi.org/10.1016/j.apcatb.2017.11.014.

[4] M. Konsolakis, Recent advances on nitrous oxide (N_2O) decomposition over non-noble-metal oxide catalysts: catalytic performance, mechanistic considerations, and surface chemistry aspects, ACS Catal. 5 (2015) 6397–6421, https://doi.org/10.1021/acscatal.5b01605.

[5] F. Lin, T. Andana, Y. Wu, J. Szanyi, Y. Wang, F. Gao, Catalytic site requirements for N_2O decomposition on Cu-, Co-, and Fe-SSZ-13 zeolites, J. Catal. 401 (2021) 70–80, https://doi.org/10.1016/j.jcat.2021.07.012.

[6] T. Schaub, Producing adipic acid without the nitrous oxide, Science 366 (2019) 1447, doi: 10.1126/science.aaz6459.

[7] E.A. Davidson, D. Kanter, Inventories and scenarios of nitrous oxide emissions, Environ. Res. Lett. 9 (2014), 105012, https://doi.org/10.1088/1748-9326/9/10/105012.

[8] J. Flückiger, A. Dällenbach, T. Blunier, B. Stauffer, T.F. Stocker, D. Raynaud, J. M. Barnola, Variations in atmospheric N_2O concentration during abrupt climatic changes, Science 285 (1999) 227–230, https://doi.org/10.1126/science.285.5425.227.

[9] M.L. Bols, B.E.R. Snyder, H.M. Rhoda, P. Cnudde, G. Fayad, R.A. Schoonheydt, V. Van Speybroeck, E.I. Solomon, B.F. Sels, Coordination and activation of nitrous oxide by iron zeolites, Nat. Catal. 4 (2021) 332–340, https://doi.org/10.1038/s41929-021-00602-4.

[10] J. Pérez-Ramírez, F. Kapteijn, K. Schöffel, J.A. Moulijn, Formation and control of N_2O in nitric acid production: Where do we stand today? Appl. Catal. B 44 (2003) 117–151, doi: 10.1016/S0926-3373(03)00026-2.

[11] J. Pérez-Ramírez, Prospects of N_2O emission regulations in the European fertilizer industry, Appl. Catal. B 70 (2007) 31–35, https://doi.org/10.1016/j.apcatb.2005.11.019.

[12] M. Galle, D.W. Agar, O. Watzenberger, Thermal N_2O decomposition in regenerative heat exchanger reactors, Chem. Eng. Sci. 56 (2001) 1587–1595, https://doi.org/10.1016/S0009-2509(00)00386-9.

[13] R. Zhang, N. Liu, Z. Lei, B. Chen, Selective transformation of various nitrogen-containing exhaust gases toward N_2 over zeolite catalysts, Chem. Rev. 116 (2016) 3658–3721, https://doi.org/10.1021/acs.chemrev.5b00474.

[14] K. Liu, X. Zhao, G. Ren, T. Yang, Y. Ren, A.F. Lee, Y. Su, X. Pan, J. Zhang, Z. Chen, J. Yang, X. Liu, T. Zhou, W. Xi, J. Luo, C. Zeng, H. Matsumoto, W. Liu, Q. Jiang, K. Wilson, A. Wang, B. Qiao, W. Li, T. Zhang, Strong metal-support interaction promoted scalable production of thermally stable single-atom catalysts, Nat. Commun. 11 (2020) 1263, https://doi.org/10.1038/s41467-020-14984-9.

[15] M. Zabilskiy, P. Djinović, E. Tchernychova, O.P. Tkachenko, L.M. Kustov, A. Pintar, Nanoshaped CuO/CeO_2 materials: effect of the exposed ceria surfaces on catalytic activity in N_2O decomposition reaction, ACS Catal. 5 (2015) 5357–5365, https://doi.org/10.1021/acscatal.5b01044.

[16] N. Richards, J.H. Carter, E. Nowicka, L.A. Parker, S. Pattisson, Q. He, N.F. Dummer, S. Golunski, G.J. Hutchings, Structure-sensitivity of alumina supported palladium catalysts for N_2O decomposition, Appl. Catal. B 264 (2020), 118501, https://doi.org/10.1016/j.apcatb.2019.118501.

[17] C. Sui, T. Zhang, Y. Dong, F. Yuan, X. Niu, Y. Zhu, Interaction between Ru and Co_3O_4 for promoted catalytic decomposition of N_2O over the Ru_x-Co_3O_4 catalysts, Mol. Catal. 435 (2017) 174–181, https://doi.org/10.1016/j.mcat.2017.03.033.

[18] M.-X. Xu, H.-X. Wang, H.-D. Ouyang, L. Zhao, Q. Lu, Direct catalytic decomposition of N_2O over bismuth modified NiO catalysts, J. Hazard. Mater. 401 (2021), 123334, https://doi.org/10.1016/j.jhazmat.2020.123334.

[19] Q. Shen, M. Wu, H. Wang, N. Sun, C. He, W. Wei, The influence of desilication on high-silica MFI and its catalytic performance for N_2O decomposition, Appl. Surf. Sci. 441 (2018) 474–481, https://doi.org/10.1016/j.apsusc.2018.01.052.

[20] C. Moreau, Á. Caravaca, P. Vernoux, S. Gil, A new dynamic approach for N_2O decomposition by pre-reduced $Rh/CeZrO_x$ catalysts, ChemCatChem 12 (2020) 3042–3049, https://doi.org/10.1002/cctc.202000242.

[21] Y. Li, A. Sundermann, O. Gerlach, K.-B. Low, C.C. Zhang, X. Zheng, H. Zhu, S. Axnanda, Catalytic decomposition of N_2O on supported Rh catalysts, Catal. Today 355 (2020) 608–619, https://doi.org/10.1016/j.cattod.2019.04.063.

[22] S. Xiong, J. Chen, N. Huang, S. Yang, Y. Peng, J. Li, Balance between reducibility and N_2O adsorption capacity for the N_2O decomposition: Cu_xCo_y catalysts as an example, Environ. Sci. Tech. 53 (2019) 10379–10386, https://doi.org/10.1021/acs.est.9b02892.

[23] P.J. Smeets, M.H. Groothaert, R.M. van Teeffelen, H. Leeman, E.J.M. Hensen, R. A. Schoonheydt, Direct NO and N_2O decomposition and NO-assisted N_2O decomposition over Cu-zeolites: Elucidating the influence of the CuCu distance on oxygen migration, J. Catal. 245 (2007) 358–368, https://doi.org/10.1016/j.jcat.2006.10.017.

[24] G. He, B. Zhang, H. He, X. Chen, Y. Shan, Atomic-scale insights into zeolite-based catalysis in N_2O decomposition, Sci. Total Environ. 673 (2019) 266–271, https://doi.org/10.1016/j.scitotenv.2019.03.481.

[25] X. Hu, Y. Wang, R. Wu, L. Zhao, X. Wei, Y. Zhao, Effects of zirconia crystal phases on the catalytic decomposition of N_2O over Co_3O_4/ZrO_2 catalysts, Appl. Surf. Sci. 514 (2020), 145892, https://doi.org/10.1016/j.apsusc.2020.145892.

[26] E. Moharramzadeh Goliaei, N. Seriani, N_2O decomposition on Ti_3O_6 deposited on anatase(101) from first-principles calculations: The role of oxygen vacancy, Appl. Surf. Sci. 579 (2022), 152215, https://doi.org/10.1016/j.apsusc.2021.152215.

[27] R. Gholizadeh, Y.-X. Yu, Y. Wang, N_2O adsorption and decomposition over ZnO (0001) doped graphene: Density functional theory calculations, Appl. Surf. Sci. 420 (2017) 944–953, https://doi.org/10.1016/j.apsusc.2017.05.235.

[28] H. Chen, Q. Lu, C. Yi, B. Yang, S. Qi, Design of bimetallic Rh-M catalysts for N_2O decomposition: From DFT calculation to experimental study, Mol. Catal. 446 (2018) 1–9, https://doi.org/10.1016/j.mcat.2017.12.008.

[29] B.M. Abu-Zied, A.M. Asiri, The role of alkali promoters in enhancing the direct N_2O decomposition reactivity over NiO catalysts, Chinese, J. Catal. 36 (2015) 1837–1845, https://doi.org/10.1016/S1872-2067(15)60963-9.

[30] K. Kim, S. Baek, J.J. Kim, J.W. Han, Catalytic decomposition of N_2O on Pd_xCu_y alloy catalysts: A density functional theory study, Appl. Surf. Sci. 510 (2020), 145349, https://doi.org/10.1016/j.apsusc.2020.145349.

[31] H. Chen, Q. Lu, C. Yi, B. Yang, S. Qi, Bimetallic Rh–Fe catalysts for N_2O decomposition: effects of surface structures on catalytic activity, Phys. Chem. Chem. Phys. 20 (2018) 5103–5111, https://doi.org/10.1039/C7CP08562A.

[32] P. Maitarad, S. Namuangruk, D. Zhang, L. Shi, H. Li, L. Huang, B. Boekfa, M. Ehara, Metal–porphyrin: a potential catalyst for direct decomposition of N_2O by theoretical reaction mechanism investigation, Environ. Sci. Tech. 48 (2014) 7101–7110, https://doi.org/10.1021/es405767d.

[33] M. Vakili, R. Gholizadeh, A. Ghadi, E. Salmasi, M. Sinnokrot, Computational investigation of N_2O adsorption and dissociation on the silicon-embedded graphene catalyst: A density functional theory perspective, J. Mol. Graph. Model. 101 (2020), 107752, https://doi.org/10.1016/j.jmgm.2020.107752.

[34] W. Qu, P. Wang, M. Gao, J.-Y. Hasegawa, Z. Shen, Q. Wang, R. Li, D. Zhang, Delocalization effect promoted the indoor air purification via directly unlocking the ring-opening pathway of toluene, Environ. Sci. Tech. 54 (2020) 9693–9701, https://doi.org/10.1021/acs.est.0c02906.

[35] X. Zhang, J. Deng, T. Lan, Y. Shen, W. Qu, Q. Zhong, D. Zhang, Coking- and sintering-resistant Ni nanocatalysts confined by active BN edges for methane dry reforming, ACS Appl. Mater. Interfaces 14 (2022) 25439–25447, https://doi.org/10.1021/acsami.2c04149.

[36] G. Kresse, J. Furthmüller, Efficiency of ab-initio total energy calculations for metals and semiconductors using a plane-wave basis set, Comput. Mater. Sci. 6 (1996) 15–50, https://doi.org/10.1016/0927-0256(96)00008-0.

[37] J.P. Perdew, K. Burke, M. Ernzerhof, Generalized gradient approximation made simple, Phys. Rev. Lett. 77 (1996) 3865–3868, https://doi.org/10.1103/PhysRevLett.77.3865.

[38] M. Capdevila-Cortada, Z. Łodziana, N. López, Performance of DFT+U approaches in the study of catalytic materials, ACS Catal. 6 (2016) 8370–8379, https://doi.org/10.1021/acscatal.6b01907.

[39] V. Wang, N. Xu, J.-C. Liu, G. Tang, W.-T. Geng, VASPKIT: A user-friendly interface facilitating high-throughput computing and analysis using VASP code, Comput. Phys. Commun. 267 (2021), 108033, https://doi.org/10.1016/j.cpc.2021.108033.

[40] X. Zhou, B. Zhu, Y. Sun, J. Chen, X. Geng, M. Xu, Insight into the N_2O formation mechanism on the β-MnO_2 (110) during low-temperature NH_3-SCR: Reaction pathway and electronic analysis of different intermediates, Appl. Surf. Sci. 607 (2023), 154981, https://doi.org/10.1016/j.apsusc.2022.154981.

[41] J. Zhou, P. Wang, A. Chen, W. Qu, Y. Zhao, D. Zhang, NO_x reduction over smart catalysts with self-created targeted antipoisoning sites, Environ. Sci. Tech. 56 (2022) 6668–6677, https://doi.org/10.1021/acs.est.2c00758.

[42] S. Maintz, V.L. Deringer, A.L. Tchougreeff, R. Dronskowski, LOBSTER: A tool to extract chemical bonding from plane-wave based DFT, J. Comput. Chem. 37 (2016) 1030–1035, https://doi.org/10.1002/jcc.24300.

[43] G. Henkelman, A. Arnaldsson, H. Jonsson, A fast and robust algorithm for Bader decomposition of charge density, Comput. Mater. Sci. 36 (2006) 354–360, https://doi.org/10.1016/j.commatsci.2005.04.010.